Physica Medica 60 (2019) 100–110

Contents lists available at ScienceDirect

Physica Medica

journal homepage: www.elsevier.com/locate/ejmp

Original paper

A method to measure slice sensitivity profiles of CT images under low-contrast and high-noise conditions

Mitsunori Goto[a,b,*], Chiaki Tominaga[a,c], Masaaki Taura[d], Hiroki Azumi[e], Kazuhiro Sato[a], Noriyasu Homma[a], Issei Mori[a]

[a] Graduate School of Medicine, Tohoku University, Sendai 980-8575, Japan
[b] Miyagi Cancer Center Natori, 981-1293, Japan
[c] Chiba University Hospital, Chiba 260-8677, Japan
[d] Tohoku Medical and Pharmaceutical University Hospital, Sendai 983-8512, Japan
[e] Sendai Medical Center, Sendai 983-8520, Japan

ARTICLE INFO

Keywords:
Slice sensitivity profile
CT
Low contrast-to-noise ratio
Iterative reconstruction

ABSTRACT

Noise reduction features of iterative reconstruction (IR) methods in computed tomography might accompany the sacrifice of the longitudinal resolution, or slice sensitivity profile (SSP), at low contrast-to-noise ratio (CNR) conditions. To assess the benefit of IR methods correctly, the difference of SSP between IR methods and filtered-backprojection (FBP) must be taken into account. Therefore, SSP measurement under low-CNR conditions is necessary. Although edge methods are predominantly used, their performance under low-CNR conditions appears to be not fully established. We developed a method that is compatible with extremely low-CNR conditions. Thin plastic disk-shaped sheets embedded in acrylic resin were used as low-contrast test objects. The lowest peak contrast used was approximately 17 [HU]. We assessed the performance of our method by using FBP images. We identified a source of measurement instability aside from noise: the measured thin-slice SSP is dependent on the orbital phase of helical scan, presumably because of cone–beam artifacts. This impediment to high accuracy is manageable using phase-controlled scans. We confirmed that table position repeatability is much better than the value of the specifications, and therefore the ensemble-averaged images of multiple scans can be used for SSP measurement. Accurate measurement of SSP under extremely low-CNR conditions is possible, even when the test object is visually indiscernible from the noisy background. Low-contrast SSP behavior is elucidated for IR methods (AIDR-3D, FIRST, and AiSR-V) by using this measurement method.

1. Introduction

Noise and resolution are important physical indexes for the assessment of the quality of computed tomography (CT) images. Generally, modulation transfer function (MTF) and slice sensitivity profile (SSP) are used respectively for the assessments of in-plane resolution and longitudinal resolution [1–4]. Noise power spectrum (NPS) is primarily used for the assessment of noise [4,5]. All these indexes are linear metrics which assume linearity of the imaging system. When this assumption is violated, they become dependent on various imaging conditions. In other words, they behave nonlinearly. Particularly, MTF and SSP may change from one imaging object to another. They may be most likely dependent on the object contrast. They also may have dependence on the noise level. However, recent iterative reconstruction (IR) methods and hybrid IR methods, designated collectively as IR methods [6], are nonlinear. Their image quality indexes are heavily dependent on the radiation dose, object contrast, and other factors [7–11]. Actually, there are basically two streams of physical image quality assessment. One is the traditional Fourier-based approach which operates in the spatial frequency domain using the MTF and NPS. Another is the spatial domain approach which typically uses channelized Hotelling observers (CHO) for task-based image quality assessment, such as the detection of small low contrast objects [12,13]. Although the spatial domain approach is theoretically more valid when nonlinear reconstruction methods are used and image quality indexes behave nonlinearly, it requires considerable time and effort. Therefore, the Fourier-based approach is still the mainstream to assess the quality of images reconstructed with nonlinear methods.

The MTF of CT images reconstructed with nonlinear methods is measured under low contrast-to-noise ratio (CNR) conditions,

* Corresponding author at: 981-1293, Nodayama 47-1 Medesima-shiode, Natori, Miyagi, Japan.
E-mail address: Goto.mitsunori@gmail.com (M. Goto).

https://doi.org/10.1016/j.ejmp.2019.03.010
Received 27 May 2018; Received in revised form 3 March 2019; Accepted 11 March 2019
Available online 30 March 2019

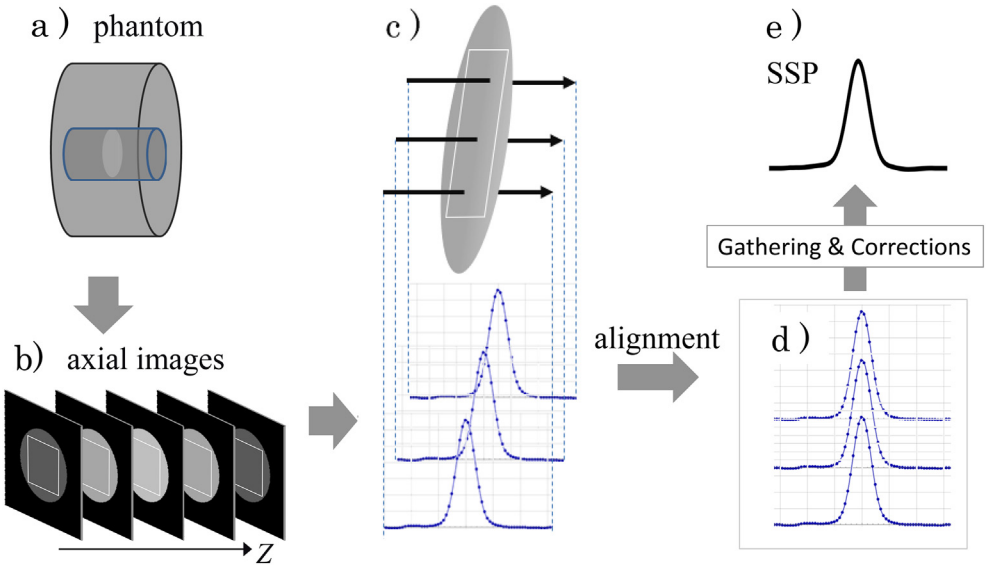

Fig. 1. Conceptual procedure of our SSP measurement method. (a) A disk phantom in water is scanned helically. (b) An ROI is set on axial images. (c) CT number profiles of pixels are mutually misaligned because of possible disk angle. The profiles depicted here are clean for illustrative purposes: they are extremely noisy in reality. Furthermore, although only three profiles are shown here, there are hundreds of profiles. (d) All profiles are aligned. (e) Gathering all profiles forms a clean SSP.

according to task-based approaches [7,8,10]. It is measured predominantly using edge methods that observe the edge response of a test object [7,8,14–17], although a method that uses indistinct impulse test objects has emerged [18]. Whatever method chosen, the MTF measurement at sufficiently low CNR is necessarily hindered by noise. However, it is manageable by use of an averaged image for which the noise level is lowered [18–20].

The SSP also must be measured at low-CNR conditions along with the measurement of in-plane properties because noise reduction in most IR methods may be accompanied by the compromise of low-CNR SSP [10,21]. Indeed, the SSPs of some IR methods were observed as being worsened under either high-noise or low-contrast conditions [22,23]. This low-CNR SSP thickening has been, in most if not all cases, neglected for the evaluation of the efficacy and dose reduction potential of IR methods. This will result in an overestimation of the image quality improvement obtained with IR methods [21], no matter whether the image quality assessment approach is in the spatial frequency domain or in the spatial domain. Similarly to the case of low-CNR MTF measurement, the SSP under low-CNR conditions is predominantly measured using edge methods. Its test object is a plastic cylinder with flat edges which is embedded in a different material of similar attenuation coefficient. The contrast difference at the edge forms a sharp step function along the longitudinal direction. SSP is obtained by differentiating the edge response profile. However, the accuracies of the obtained SSPs of these reports were not fully established, especially with respect to robustness against noise. In the reported edge methods [22,23], the lowest contrast levels tested were 120–205 HU, which are substantially higher than the level of soft-tissue contrasts.

The philosophy of task-based assessment states that the resolution must be measured under specific conditions similar to a specific clinical task [7,8]. SSP measurement is no exception. In this sense, the contrast levels required for the test objects of the edge method are too high to reflect human organs or lesions. Furthermore, the image quality improvement of indistinct objects may be clinically more valuable than that of already distinct objects. From this point of view, test objects used for the edge method are generally too distinct. An ideal SSP measurement method should be compatible with extremely low-CNR conditions, where the test object is not distinctly visible against a noisy background.

One can easily conceive the use of ensemble-averaged images from multiple scans. Then, the difficulty in low-CNR SSP measurement can be mitigated by the reduction of image noise level. However, the table position inaccuracy in longitudinal direction is ±0.25 mm for all currently available CT systems, according to their specifications. It is too large for the use of ensemble-averaged images to measure the SSP of the thin slice accurately. We cannot casually rely on ensemble averaging, unlike in the case of low-CNR MTF measurement.

Two other issues exist in the pre-existing low-CNR SSP measurement methods. First, the obtained SSPs might be affected by the cone–beam artifact. The test object is relatively large, with abrupt changes in the longitudinal direction. The images near the edge of such an object are contaminated by cone–beam artifacts, depending on the relative position of the test object against a helical scan orbit. This potential difficulty has remained uninvestigated.

Second, SSP using the edge methods is obtained through differentiation of the blurring of the object edge. When the linearity of the system is not guaranteed, some concern might arise regarding whether such SSP is the same as the orthodox SSP, which is defined as the longitudinal response to the impulse object. A more direct mode of measurement, which uses a longitudinal impulse test object, might be preferred.

Considering the points mentioned above, we have developed and evaluated a new method for SSP measurement that is compatible with very low-CNR conditions. The accuracy of the proposed method is examined at various CNR levels. Accurate SSP is obtainable even at extremely low-CNR conditions where the test object is indistinct against a noisy background. For that purpose, the pre-existing edge method is discarded. Instead, thin plastic low-contrast disk is used as a longitudinal impulse test object.

2. Materials and methods

We first describe our low-CNR SSP measurement method, and then evaluate its accuracy at various CNR levels using images reconstructed by filtered backprojection (FBP).

After the validation of the measurement accuracy, we apply our method to IR methods to ascertain whether it is effective enough to represent their SSP performance.

2.1. SSP measurement method

2.1.1. Conceptual explanation

A conceptual description of our method is depicted in Fig. 1.

We use low-contrast thin plastic disks embedded in acrylic resin as our test phantom.

The phantom is set in a water vessel so that its axis is parallel to the rotation axis of the scanner, although a slight tilting angle of the disk is unavoidable. Regular-pitched axial images are obtained by helical

scanning. A region of interest (ROI) is set in the axial images. Each pixel within the ROI constitutes a z-directional CT number profile. The profiles have their own z-directional shift depending on the pixel position because of the finite tilting of the disk. The position and tilting angle of the disk can be detected precisely by assessing the entire images. Accordingly, the profiles are precisely aligned in the z-direction. The aligned profiles are combined to form a single profile.

The combined profile is highly inaccurate because of noise. However, a binning process is applied to form a regular-pitched and noise-suppressed profile. Then, after careful base-level correction, width correction is applied because the obtained profile is thickened slightly by a few factors such as the finite disk thickness. The details of data processing are presented in the Appendix.

2.1.2. SSP phantom

To improve test efficiency, we built a multi-contrast phantom so that the SSPs of multiple contrast levels can be obtained by a single scan. The materials and thicknesses of the plastic disks were polyethylene terephthalate (PET) 0.2 mm, PET 0.3 mm, polyoxymethylene (POM) 0.3 mm, and polyvinyl chloride (PVC) 0.2 mm from the lowest contrast to the highest contrast. Hereinafter, they are denoted as PET0.2, PET0.3, POM0.3, and PVC0.2.

The peak contrast of the disk image against acrylic resin, or the height of obtained SSP, is dependent on various scanning and reconstruction parameters. However, in this study using FBP images, the typical peak contrasts for 0.5-mm slice thickness are approximately 17, 34, 60, and 162 [HU], respectively, for PET0.2, PET0.3, POM0.3, and PVC0.2. Hereinafter, we use the peak-contrast-to-noise ratio (pCNR), which is the ratio of the profile peak to the standard deviation of the background noise, as the main parameter to describe the measurement condition.

The disk diameters were larger for lower contrast and smaller for higher contrast, based on the consideration of tradeoff between noise and cone-beam artifact tolerance: 30, 25, 20 and 15 mm for PET0.2, PET0.3, POM0.3, and PVC0.2, respectively.

Large disks are beneficial from the perspective of noise: the SSP obtained from higher number of pixels benefits from a stronger averaging effect. However, abrupt changes in the longitudinal direction cause cone–beam artifacts that are stronger for large structures [24]; disks are no exception. We want a genuine artifact-free SSP which can be obtained by using sufficiently small test object, while combating noise. We assigned importance to noise suppression for lower contrast disks that are susceptible to noise.

Ideally, all disks should be orthogonal to the phantom axis. However, they might be tilted by a small angle (approximately 0.2° or 0.3°) because of imperfections in fabrication. Furthermore, the phantom axis cannot be set perfectly parallel to the rotation axis of the scanner. Therefore, the disks have a finite tilting angle that might reach nearly 1°. This tilting is handled properly in the data processing as shown in the Appendix.

Metal lock (Cemedine Co. Ltd.), whose CT number is only slightly lower than that of acrylic resin, was used to bond the plastic disks with acrylic cylinders. Entrapment of air bubbles in the adhesion layer was carefully avoided during the fabrication process.

This phantom is intended for thin slices. Although the SSP of the thin slice well diminishes to zero at a few millimeters from the center, we maintained a distance of 8 mm or more from the disk to the joint because a certain range of data beyond the end of the SSP is necessary for base-level correction, as explained in the Appendix.

2.1.3. Control of orbital phase of helical scan and use of anti-phased pair

In this paper, helical scans were performed with control of the orbital phase, because the observed SSP might be dependent on the relative position of the disk to the orbit of the helical scan. We express the helical scan orbit in terms of the orbital phase, which is defined as the rotation angle of the X-ray source when the source reaches the longitudinal position of the disk. Although we cannot control the orbital phase of individual scans, we can control the difference between the orbital phases of repetitive scans by proper time scheduling of the dynamic scan as proposed by Yamashita [25]. It is explained below.

When repetitive scans are performed based on a time schedule, an arbitrary orbital phase difference $\Delta\phi$ between adjacent scans is achieved by choosing their time interval Δt as given in Eqs. (1) and (2).

$$\Delta t = \frac{\Delta\phi}{2\pi} T_{rot} + NT_{rot} \tag{1}$$

$$NT_{rot} > T_{cycle} \tag{2}$$

T_{rot} denotes the time for one rotation. T_{cycle} is scanner dependent and denotes the minimum cycle time for the repetitive scans of a given longitudinal range. N in Eq. (2) is an arbitrary integer. However, we avoided an unnecessarily large value for N, because the actual T_{rot} might be slightly different from its nominal value. The accumulation of slight difference during N rotations might cause deviation of $\Delta\phi$ from the planned value.

In our experience, Δt between the first and second scans was always found to be randomly different from the planned value. The maximum difference reached to near half of T_{rot}. Therefore, we performed $1 + M$ repetitive scans when we needed M repetitive scans, and then discarded the first scan.

When the dependence on the orbital phase is not negligible, we propose using an anti-phased scan pair for which the orbital phase mutually differs by π radian as a solution. Their orbital phase dependence should be canceled out if both data were combined properly.

2.2. Evaluation methods

The main issue is the evaluation of the accuracy of measured SSP at low-CNR conditions. However, if the accuracy might be impaired by the dependence of the SSP on the orbital phase, then we must manage this effect. Furthermore, the possibility exists that the repeatability of the table position is sufficiently good for the use of ensemble-averaged images, which augments the robustness against noise, because the value ± 0.25 mm of the specifications may only be applicable to the worst case amongst all possible usages of the scanner.

Therefore, the evaluation of the measurement accuracy of low-CNR SSP was performed together with the issues of the orbital phase and the table position repeatability.

2.2.1. CT system and conditions

We used Aquilion One™ (Toshiba Medical Systems Corp.) as the CT system to evaluate our SSP measurement method. The SSP phantom was placed in a 180-mm-diameter water vessel. It was set approximately at the isocenter of the scanner. This phantom position was kept the same throughout the study so that SSP's position dependence in an axial plane does not contaminate our measurement. Centers of all disks were retrospectively identified to be within 3 mm from the isocenter of the scanner for all cases. The scan conditions were as follows, unless otherwise noted: 120 kV tube voltage; 20, 50, 100, 150, and 300 mA tube current; 1 s per rotation; collimation width 0.5 mm; 64 rows; helical scan with pitch factor of 0.828. We performed either six consecutive scans or six anti-phased scan pairs, as will be detailed in Section 2.2.3.

Image reconstruction conditions were as follows: reconstruction field of view 320 mm; nominal slice thickness 0.5 mm; slice spacing 0.1 mm; FBP with FC13 kernel. All optional processing, such as functionalities designated as Boost3D and Sure IQ, which affect the SSP, were disabled.

The background noise standard deviations were 27, 17, 12, 9.9, and 7.1 [HU], for tube current of 20, 50, 100, 150, and 300 mA, respectively. They were measured at the proximity of SSP phantom in the water vessel, using square ROI of 40 × 40 pixels for all slices.

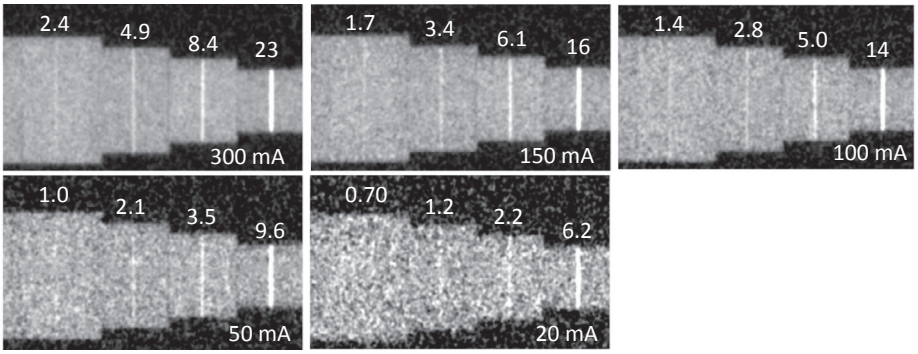

Fig. 2. Disk visibility in a sagittal section at various levels of pCNR, in the FBP case. Disks are PET0.2, PET0.3, POM0.3, and PVC0.2, from left to right. Values near the disks are the observed pCNR levels. WL and WW are 100 and 200 [HU].

The sagittal section of the phantom is depicted in Fig. 2, which shows the visibility of the disks at the above noise levels. Images and pCNR levels in Fig. 2 may give an instinctive feel for our test conditions of low-CNR SSP measurement. The disks are recognizable at pCNR levels of about 5, although not clearly. Roughly speaking, in our case, they are indistinct when the pCNR is lower than 3. Our goal is the SSP measurement method that is usable even when the test object is indistinct. As will be seen in the results section, most of data will be presented using these pCNR values.

2.2.2. Operating parameters for data processing to obtain SSP

A few operating parameters exist for data processing, as explained in the Appendix. They are described below.

The sizes of the ROI $I \times J$ were 30×30, 25×25, 18×18, and 14×14 pixels (or 353, 246, 125, and 77 mm^2) for PET0.2, PET0.3, POM0.3, and PVC0.2, respectively.

The number of slices K was 140. In other words, the longitudinal span of the used images was 14 mm for each disk. Both distance d for the base-level appraisal and distance t for zeroing were 2 mm. The bin size w for binning was 0.1 mm.

2.2.3. Acquisition of images for analysis

We obtained two varieties of image data, as described below.

The first is the data to analyze the orbital phase dependence. In this case, tube current was fixed at 300 mA, which is the condition for lowest noise. We performed six consecutive helical scans for which the orbital phase increased by $\Delta\varnothing = 2\pi/5$ radian (or 72°) increments. This increase was achieved by setting the time interval Δt in Eq. (1) as 10.2 s in accordance with the orbital phase control method described previously.

The second is the main data to analyze the accuracies of the obtained low-CNR SSPs. This data is also used to analyze the repeatability of the table position or usability of ensemble-averaged images. We performed six consecutive phase-alternate helical scans for which the orbital phase changed by $\Delta\phi = \pi$ radian. The time interval Δt was 10.5 s. This data acquisition was repeated for each of five levels of tube current as presented in Section 2.2.1.

2.2.4. Evaluation: Influence of orbital phase on the obtained SSP

As explained in the previous section, we performed six consecutive helical scans at 300 mA incrementing orbital phase by $\Delta\varnothing = 2\pi/5$ radian. We obtained the SSPs from each of the four disks using the images at each of the six orbital phases. Then, the phase dependency of obtained SSP was analyzed.

2.2.5. Evaluation: repeatability of the table position

We evaluated the repeatability of the table position for use of ensemble-averaged images, by using intermediate products of the alignment procedure as an indicator of the table position.

As explained in the Appendix, the longitudinal coordinate $k_C(i, j)$ of a disk within the three-dimensional ROI, with size of $K \times I \times J$, can be detected accurately. Scan-by-scan variation in $k_C(i, j)$ directly reflects the variation in the table position. Below, z_c is the z-coordinate of the detected disk, defining the center of the span K as the origin of the z-coordinate. Δz is the slice spacing in millimeters. The coordinate (i,j) of $k_C(i, j)$ is fixed at the center of the in-plane ROI of $I \times J$.

$$z_c = (k_C(I + 1/2, J + 1/2) - (K + 1)/2)\Delta z \tag{3}$$

As explained in Section 2.2.3, the same dynamic scan was repeated for six times with phase-alternating at each of the five tube current levels. We evaluated the change in z_c during the course of six consecutive scans for each of the five runs. For this purpose, we used the disk of PVC0.2 which has the highest contrast.

2.2.6. Evaluation: accuracy of measured SSP at low-CNR conditions

The evaluation of SSP measurement accuracy at low-CNR conditions was executed using images obtained by six consecutive phase-alternate scans which is explained in Section 2.2.3. The same image data were used commonly in three different ways to obtain SSPs, as described below.

First, we obtained the SSPs by using the images of individual scans with ignoring the alternated phase. Four disks of each peak contrast and five levels of tube current constitute 20 pCNR levels. Therefore, we obtained six SSPs for each of the 20 levels of pCNR.

Second, we obtained the combined SSPs from anti-phased scan pairs. Actually, we used simple averaging of two SSPs using the above SSPs of the individual scans, as follows. Denoting the SSP obtained from the m-th phase-alternate scan as SSP_m, we took the averages of SSP_1 and SSP_2, SSP_2 and SSP_3, SSP_3 and SSP_4, SSP_4 and SSP_5, and SSP_5 and SSP_6. Therefore, we obtained five SSPs for each of the 20 pCNR levels.

Third, we performed the SSP measurement using the ensemble-averaged images. An ensemble-averaged image $\bar{I}_n$ of the n-th slice is defined as below, where I_{mn} denotes the image of the n-th slice of the m-th scan.

$$\bar{I}_n = \frac{1}{6}\sum_{m=1}^{6} I_{mn} \tag{4}$$

A set of ensemble-averaged images was generated from the images of six consecutive phase-alternate scans for each of the five tube current levels. The SSPs were obtained for each disk. Therefore, we obtained one SSP for each of the 20 pCNR levels. Note that the noise level of ensemble-averaged images is inversely proportional to the $\sqrt{M}$, where M is the number of repetitive scans. When the measurement error is governed by the stochastic noise, and a certain level of accuracy is obtainable at a pCNR level of X by single scan, the same level of statistical accuracy can be expected at the pCNR level of $X/\sqrt{M}$ by M scans. M is chosen arbitrarily depending on the desired degree of noise reduction. In this test, M is six. Although the noise reduction factor $\sqrt{6}$

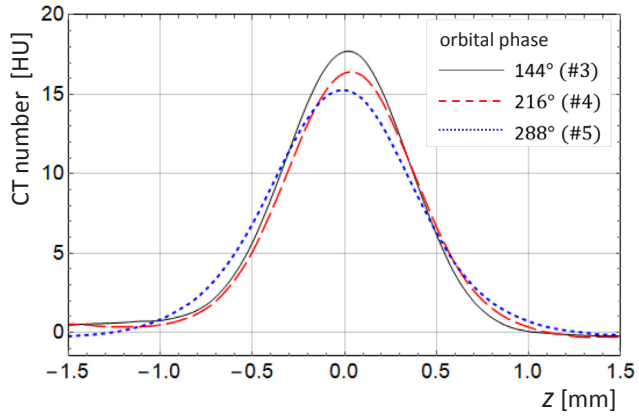

Fig. 3. The obtained SSPs are dependent on the phase of the helical scan orbit. SSPs of PET0.2 for scan Nos. 3, 4, and 5 are shown. FBP images were used. Phase angles in the legend are relative values assuming that the phase of the first scan is 0°.

is modest, its benefit should be observable if the SSP measurement error is governed by the stochastic noise.

2.2.7. Evaluation: reference SSP at high-CNR condition

The ground truth, or the reference SSP, is needed to assess the accuracy of the obtained SSPs. For this purpose, we measured an SSP under high-CNR condition using the conventional micro-disk (or micro-coin) method [26,27]. The test phantom used here was a high-contrast micro-coin phantom (Kyoto Kagaku Co. Ltd.) set in the air. The tube current was 300 mA. Other conditions were the same as those described in Section 2.2.1. The pCNR value was approximately 600. The obtained FWHM was 0.817 mm.

2.3. Application to IR methods

2.3.1. Used IR methods and CT systems

Among many IR methods, we chose three methods whose SSP seemed compromised at low-CNR conditions. One was a hybrid IR method dubbed "AIDR-3D" [28–31] installed in the Aquilion One that was the identical CT system used in Section 2.2. The second was a model-based IR method dubbed "FIRST" [29–31] that was installed in a yet another Aquilion One at a different facility. The third was a hybrid IR method dubbed "ASIR-V" [32–34] of Revolution Evo™ (GE Healthcare).

Actually, there are several operation modes for each IR method. We chose STRONG mode for AIDR-3D, BODY mode for FIRST, and 100% mode for ASIR-V.

2.3.2. Measurement conditions

Conditions of SSP measurement were similar to that described previously. However, there were several differences as explained below. Other unspecified conditions were the same as Section 2.2.

Tube current was set at 300, 50 and 10 mA. Collimation width for ASIR-V was 0.625 mm. Number of rows for FIRST was 40. Helical scan was performed with pitch factor of 0.75 for AIDR-3D, 0.97 for FIRST, and 0.98 for ASIR-V. These values, except for the tube current, were chosen so as to conform to the clinical conditions for abdominal thin-slice imaging employed at each facility.

We used ensemble averaging of multiple helical scans fully for all cases to achieve the best accuracy.

Number of phase-alternate helical scans for ensemble averaging was 4 at 300 mA, 6 at 50 mA and 10 mA, for AIDR-3D.

We employed a higher number of phase-alternate scans for FIRST; 10, 16 and 32 for tube current of 300, 50, and 10 mA respectively. This is because we anticipated a difficulty of low-CNR measurement due to weakening of SSP signal by FIRST. It will be described in the results section.

For, ASiR-V, number of helical scans was as high as that for FIRST. In this case, we omitted the use of phase-alternation. Instead, random values were used for the time intervals between scans so that phase relations among scans were random. This was because the phase effect, even if it exist with Revolution Evo also, would be diluted out substantially in ensemble-averaged images, if phase relations were random and if many scans are used. This is the reason of high number of scans for ASiR-V.

SSP behavior of IR methods can be better described when stable SSP of FBP images is used as a reference. Therefore, for each CT system and for each disk, we also obtained SSPs from ensemble averaged FBP images at 300 mA. The FBP images for ensemble averaging were reconstructed utilizing the same raw data as used for IR methods.

Note that we did not make direct measurements of table position repeatability for Aquilion One equipped with FIRST and Revolution Evo with ASiR-V. However, it can be checked by comparing the SSP obtained from ensemble-averaged FBP images with reliable SSP obtained from single scan images. For that purpose, we obtained SSP of single scan FBP images by using micro-disk method at 300 mA for each CT system. As for obtaining the SSP of ensemble-averaged FBP images, we reconstructed FBP images utilizing the same raw data of aforementioned 32 consecutive scans of SSP phantom at 10 mA, and took their ensemble-averaged images.

3. Results

The low-CNR SSPs obtained in this study are too numerous to present. We have shown only a few SSPs obtained under relatively difficult conditions. Instead, we used the full width at half maximum (FWHM) values as a representative index for assessing the accuracy of the measured SSPs.

Fig. 3 exemplifies phase-dependent SSPs obtained from PET0.2 for each of the three consecutive orbital phases. The variation in the SSP is apparent. Each is distorted differently. The phase angles shown in the legend are relative values assuming that the phase of the first scan is 0° because the absolute phase angle at the position of the disk is unknown.

The phase dependence is apparent in Fig. 4, which shows the FWHMs of the obtained SSPs for each orbital phase and for each disk. Their values change by one cycle per 360° of orbital phase. The amplitude of change is more pronounced for large-diameter disks. The ratio of maximum to minimum FWHM values is 1.17 for PET0.2. The FWHM of the smallest diameter disk PVC0.2 still changes by 5%, but it is more stable. Obviously, this phase-dependent instability of SSP is a result of large disk size.

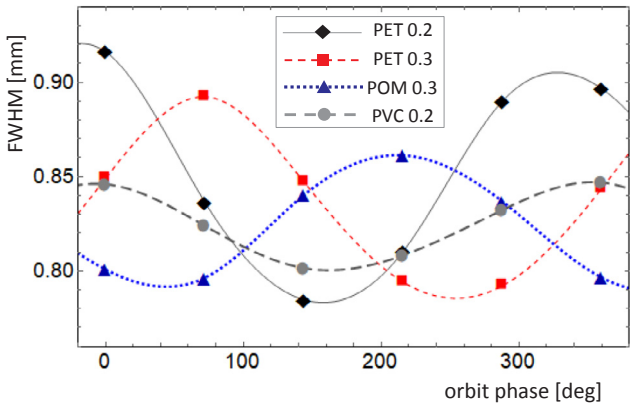

Fig. 4. Measured FWHM according to the phase of the helical orbit. FBP images were used. Horizontal axis is the orbital phase in the form of $360 \times 0.2 \times (n-1)$ degree, which is the phase difference between the n-th scan and the first scan.

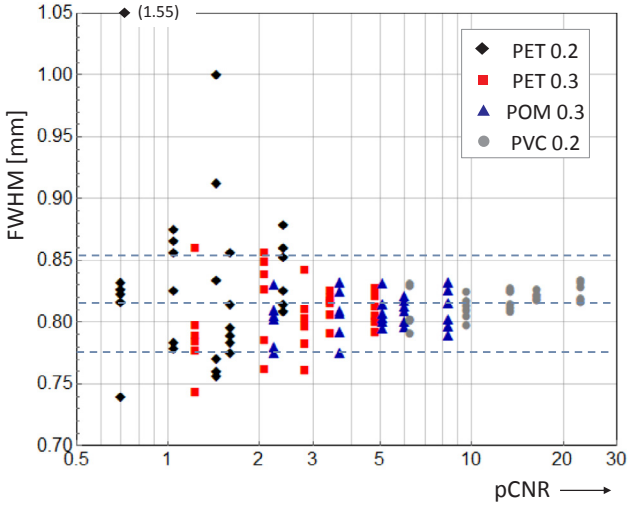

Fig. 5. Measured FWHMs of individual SSPs obtained from each of six scans at each of five tube current levels. FBP images were used. An outlier is shown at the top along with its value. The dashed horizontal lines are the reference values of the micro-disk method and its ± 5% levels.

Fig. 5 depicts the scatter diagram of the FWHMs of individual SSPs obtained from each of the six consecutive scans. Apparently, the scan-by-scan fluctuation of the FWHM is higher at lower pCNR levels. The orbital phase dependence is not yet remedied for these individual SSPs. Regarding outliers in Fig. 5, we have retrospectively identified the cause for a few extreme outliers. It was a failure of fitting process for disk position detection. Detail of the fitting failure at bad condition and its detection are explained in the Appendix.

Fig. 6 portrays a scatter diagram of the FWHMs of SSPs obtained from anti-phased pairs, which was explained in the Section 2.2.6. The fluctuation in the obtained FWHM is mitigated substantially compared to that depicted in Fig. 5. The improvement is partly attributable to the reduction of error because of stochastic noise: information of two scans is used for one SSP. However, the improvement from Figs. 5 to 6 is greater than a factor of $\sqrt{2}$, especially at relatively high pCNR levels. This is attributable to phase dependence mitigation using the anti-phased paring. Fig. 7 depicts a combination of a pair of anti-phased data. The distortions of the individual SSPs obtained from each of anti-phased scan pair are appreciably antisymmetric. The SSP obtained as

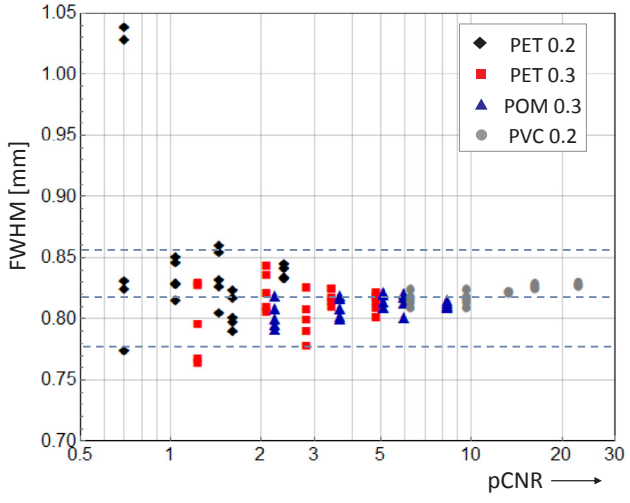

Fig. 6. Measured FWHMs of SSPs obtained from anti-phased scan pairs. Two SSPs of adjacent anti-phased scan pair were averaged to form one SSP. FBP images were used. Dashed horizontal lines represent the reference values and ± 5% levels.

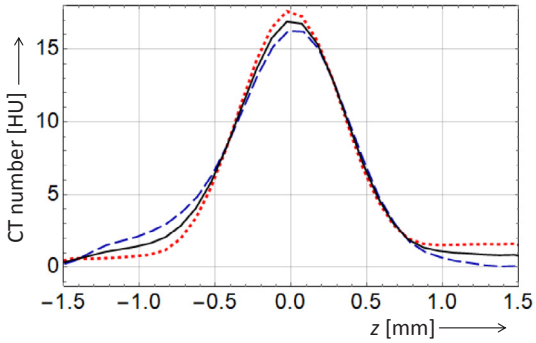

Fig. 7. Dashed and dotted lines are individual SSPs obtained from FBP images of the first and second scans, which are opposite in terms of orbital phase, of PET0.2 at 300 mA (pCNR of approximately 2.4); the FWHMs were 0.88 mm and 0.81 mm, respectively. The solid line shows their average. Its FWHM was 0.84 mm.

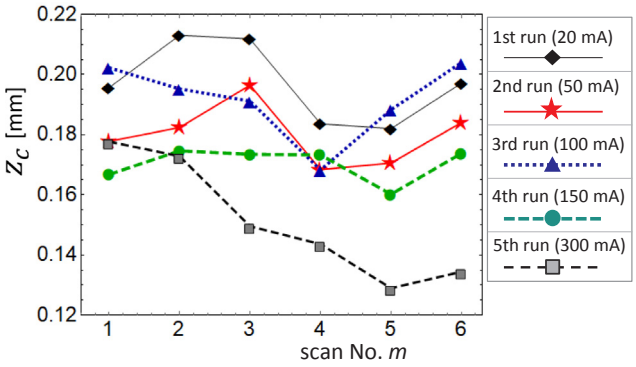

Fig. 8. Variation in the disk position z_c, which reflects the table position, during six consecutive scans. The disk positions were detected for each scan using FBP images. Results of five sets of consecutive scans are shown. The table position is more repeatable than the specification.

their average is less distorted.

Fig. 8 presents scan-by-scan repeatability of the detected disk position z_c, which is the same as the scan-by-scan repeatability of the table position. The mean level of z_c is not a concern because it depends on the ROI setting. We are interested in its repeatability. The worst case is the fifth run: the difference between the maximum and minimum values of $z_c$was 0.049 mm. In other words, the scan-by-scan table position uncertainty during the course of six repetitive scans was ± 0.025 mm. Even when all five runs are considered together, the difference between the maximum and minimum values of z_c was 0.084 mm, which is far smaller than the value ± 0.25 mm of the specification.

Fig. 9 shows the FWHMs of SSPs obtained from ensemble-averaged images, which was explained in the last part of the Section 2.2.6. All data points are well within ± 5% of the reference value. Note that the pCNR values of the ensemble averaged images are approximately $\sqrt{6}$ times these values in Fig. 9. Fig. 10 presents the worst case SSP in Fig. 9, for which the FWHM value is maximally deviated from the reference value.

Fig. 11 presents SSPs of CT systems in which FIRST and ASiR-V were implemented. However, these are SSPs of FBP images. As described in the last paragraph of Section 2.3.2, one SSP was obtained from single-scan micro-disk FBP images, and another SSP was obtained from ensemble-averaged FBP images of 32 consecutive scans. Among ensemble-averaged SSPs obtained from four different contrast disks, we here arbitrarily chose the case of PET0.2 because SSP of FBP images is contrast-independent in principle. For both CT systems, SSPs of PET0.2, obtained by using ensemble-averaged images of 32 consecutive scans, show good matches with the SSPs obtained from single-scan micro-disk

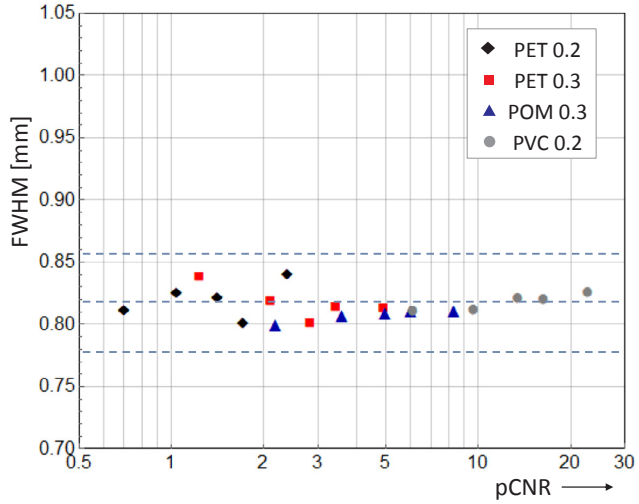

Fig. 9. Measured FWHM of SSP obtained from the ensemble-averaged FBP images of six scans. The horizontal axis shows the original pCNR levels obtained by single scan. Actual pCNR levels of the ensemble-averaged image are approximately $\sqrt{6}$ times higher. Dashed horizontal lines represent the reference value and its ± 5% levels.

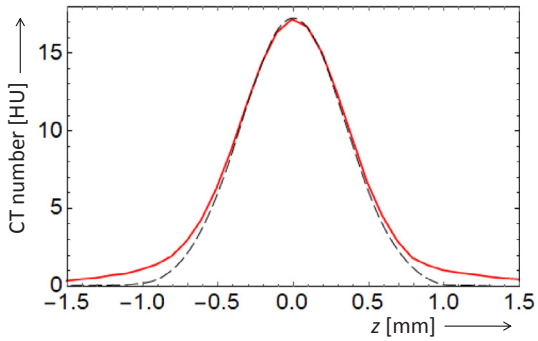

Fig. 10. The solid line is the SSP obtained from the ensemble-averaged FBP images of PET0.2 at 300 mA, for which the pCNR value was 5.6 (originally 2.4 without ensemble averaging). The thin dashed line shows the reference SSP obtained by using high-CNR micro-disk FBP images at 300 mA, but its height is adjusted to the same height as that of PET0.2.

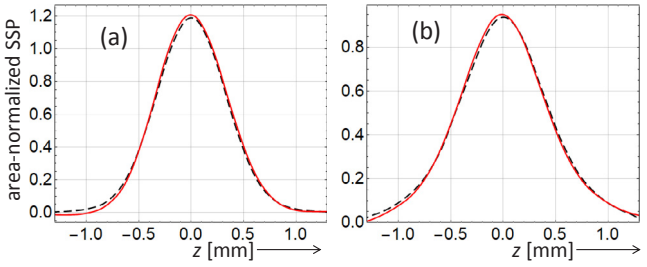

Fig. 11. The solid line is the SSP obtained by ensemble-averaged FBP images of 32 scans at 10 mA, using PET0.2. The dashed line is the reference SSP obtained by single scan using high-contrast micro-disk FBP images at 300 mA. SSP height is adjusted to the same lelvel by area normalization. (a) The Aquilion One equipped with FIRST. FWHM ratio (ensemble-averaged/reference) is 1.012 (0.789/0.779). (b) Revolution Evo equipped with ASiR-V. FWHM ratio is 0.983 (0.943/0.959).

images. The differences of FWHM are within 2%, indicating that the table position during 32 consecutive scans was repeatable enough for both CT systems. Therefore, the obtained SSPs of FIRST and ASiR-V, which are shown hereafter, are unaffected by the table position uncertainty.

Fig. 12 presents SSPs of AIDR-3D STRONG, FIRST BODY, and ASiR-V 100% for each disk and at each tube current. It is obvious that their SSPs are markedly thickened at low-contrast conditions and/or low tube current (or high-noise) conditions. Furthermore, some SSPs are notably deformed.

General trend of their thickness is visualized in Fig. 13. Here, Gaussian width is used as the metric of thickness, because FWHM cannot be a common metric of thickness for different shapes. The Gaussian width was obtained by fitting a Gaussian function to each SSP. Behaviors of three IR methods are distinctively different to each other. Basically, SSP of AIDR-3D SSP depends on the noise level but not on the contrast. FIRST BODY is strongly contrast-dependent. It blurs SSP of PET0.3 or lower contrast radically, while sharpening SSP of POM0.3 or higher contrast. ASIR-V is entirely CNR-dependent.

The low-contrast SSP of FIRST is particularly peculiar. It is deformed and the thickness reaches up to even four or five times of that of FBP. It is also peculiar in its signal strength which is the integral of SSP, or area under SSP curve. The signal strength of AIDR-3D or ASiR-V is seemingly unchanged from that of SSP of FBP according to Fig. 12. However, in the case of FIRST, the signal strength of low-contrast disks, such as PET0.2 or PET0.3, is apparently lower than that of FBP. Fig. 14 shows that the visibility of low-contrast disks is indeed seriously impaired by use of FIRST.

4. Discussion

Our goal was to obtain an accurate method for SSP measurements at extremely low-CNR conditions, with the test object indistinct against a noisy background. Our results obtained from the individual scans were such that the pCNR level must be 5 or higher (Fig. 5) if the maximum allowable error of the FWHM is assumed to be ± 5%. As presented in Fig. 2, the disks are recognizable at that pCNR level. Therefore, the performance with the single-scan method falls slightly short of our goal. Nevertheless, this performance appears superior to that of the existing edge method at substantially higher contrast levels: Chen *et al.* used 205 HU contrast and Li *et al.* used 120 HU contrast [22,23]. The improvement of the accuracy is attributable mainly to the averaging effect using the information of numerous pixels. Another factor may be involved: the edge methods require a differentiation operation, which worsens noise statistics.

We confirmed that the measured SSPs are accompanied by considerable orbital phase dependence (Fig. 4). The dependence is larger for larger disk. The root cause is supposed to be a cone–beam artifact. As a solution to cancel out the phase dependence, an SSP was obtained from a pair of anti-phased scans. The results portrayed in Fig. 6 were notably improved from those of individual scans (Fig. 5). However, the anti-phased paring alone is not satisfactory at extremely low-CNR, where the noise is the primary source of measurement error, if the FWHM is assumed to be within ± 5% of the reference value.

Results show that the table position repeatability is much better than the nominal specification when consecutive scans are used (Fig. 8). Although this direct measurement of table position was performed for only six consecutive scans, results of two other CT systems indirectly showed that their table positions were reasonably repeatable for 32 consecutive scans (Fig. 11). We speculate that the majority of CT scanners permit the use of ensemble-averaging of numerous consecutive scans even for thin-slice SSP measurement. However, it remains a speculation. That is a limitation of our study.

Ensemble averaging of six phase-alternate scans appears sufficient for our method which is already fairly robust against noise, as follows. Even when the original pCNR of an individual scan is lower than 2, where the disk is indistinct against the noisy background, the FWHM error is within ± 5% (Fig. 9). The worst case SSP portrayed in Fig. 10 is somewhat deviated from the reference profile. The deviation is particularly notable at the foot of SSP, although the FWHM error is within 5%. Granted, FWHM alone cannot be a comprehensive measure of

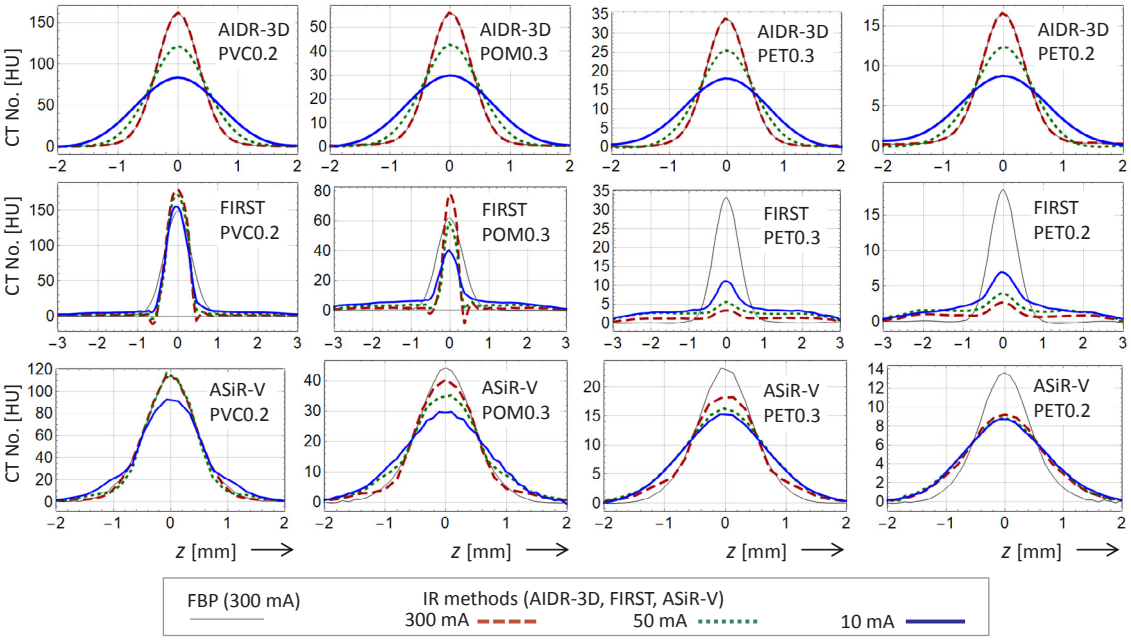

Fig. 12. Contrast- and noise-dependent SSP of IR methods (AIDR-3D STRONG, FIRST BODY, and ASiR-V 100%), at three tube current levels. For each disk, SSP obtained using FBP images at 300 mA is also shown as a reference. The range of horizontal axis is wider for FIRST because some of its SSPs are extremely widened.

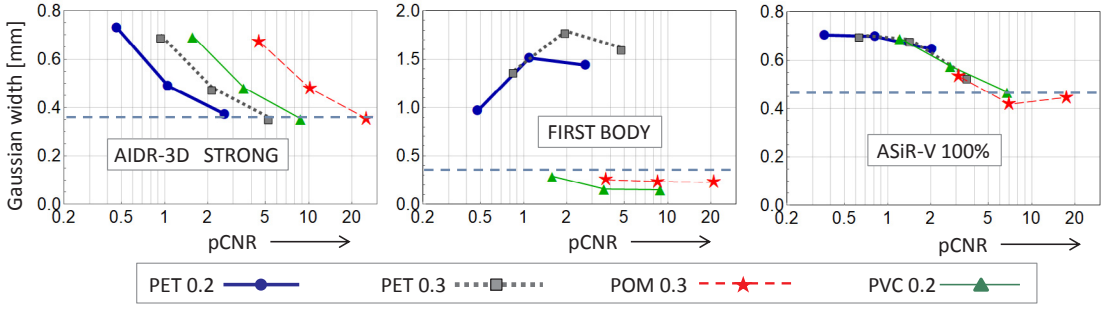

Fig. 13. SSP thickness of three IR methods. They behave very differently to each other. Gaussian width is used as an index of thickness. The horizontal axis is the original pCNR level of FBP images before ensemble-averaging. For each disk, the three distinct levels of the pCNR correspond to tube currents of 10, 50, and 300 mA, from left to right. The horizontal dashed lines show Gaussian widths of contrast-independent SSPs obtained from FBP images of PVC0.2 at 300 mA.

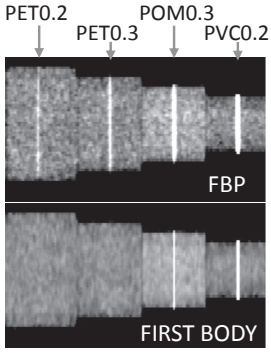

Fig. 14. A case of signal strength reduction. Low-contrast disks almost vanished when FIRST BODY is used. At 300 mA. Saggital plane of slab thickness 4 pixels (2.5 mm). WL and WW are 50 and 120 [HU].

accuracy. Nevertheless, its asymmetricity and ruggedness because of noise are far more moderate than the SSP obtained by pre-existing edge method with much higher CNR conditions [23].

We expect our SSP measurement method can be used for a detailed survey of IR methods' low-CNR SSP which is not provided by manufacturers. As exemplified in Figs. 12 and 13, the SSP behavior is totally dependent on the type of IR method; AIDR-3D is noise-dependent, FIRST is contrast-dependent, and ASiR-V is CNR-dependent. One common observation is that their SSPs are markedly thickened at conditions where the test object is not distinct enough and pre-existing edge method may not be operable. Furthermore, a peculiar signal strength reduction of low-contrast SSP was found for FIRST. These observations were possible thanks to the multi-contrast feature and the robustness under low-CNR conditions of our method, although the adjunctive use of ensemble averaging of multiple scans was required to augment the robustness against noise for extremely low-CNR conditions.

The most important use of low-CNR SSP measurement will be to make the present task-based evaluation of IR method, which is based on in-plane low-CNR resolution and in-plane NPS, more comprehensive. To correctly evaluate the benefit of IR method over the FBP, whether it truly reduces radiation dose while maintaining the detectability of indistinct object, the difference of low-CNR SSP must be correctly compensated for. However, this objective is beyond the scope of this paper.

Our method involves several seemingly complex procedures, such as alignment with disk angle detection, width correction, and anti-phased pairing. These are intended to achieve the best possible measurement accuracy of the thin-slice SSP. These procedures may be omitted depending on the situation if simplification is desired. First, all of them

might be omitted for thick slices. The effects of the disk angle, disk thickness, and orbital phase dependence become minor for thicker slices. The necessity of attention to the phase-dependence may be model-dependent for thin slices as well. If the culprit of the phase-dependence is cone-beam artifact, the phase dependence can be more moderate depending on the number of rows and details of the reconstruction algorithm employed. Another means of simplifying the procedures is the use of ensemble-averaged images of tens of random-phased scans if the repeatability of the table position is proven for numerous scans. In doing so, the disk size need not be large to combat the noise. Smaller size of the disk mitigates both effects of the finite tilting angle and the orbital phase dependence. Furthermore, the orbital phase dependence will be averaged out.

We have evaluated our SSP measurement method using the thinnest slices, because SSP is more often discussed for thin slices than thick slices. Another reason is that the measurement accuracy of SSP would be more challenging and worthy to examine at the thinnest slices, because possible subtle issues, such as the table position repeatability and the orbital phase dependency, would become more problematic. However, one may want to investigate low-CNR SSPs at far thicker slices. For that, the challenge to low-CNR condition is the same as that at thin slices, and therefore we believe the presented method can be used. Still, we have not validated it. This is a limitation of our study. At least, some modifications would be required. The distance from the disk to the joint must be wider than our presented 8 mm. Higher contrast materials or thicker sheets than those presented may be preferred because peak contrast levels are lowered by partial volume effect of thick slices. Also, a larger external water container would be more adequate than our 180 mm diameter water vessel to attain high noise at thick slices.

5. Conclusion

Thin plastic sheets were used as the low-contrast test objects for the evaluation of SSP under low-CNR conditions. The robustness against noise was superior to the pre-existing edge methods that observe the response profile of a cylinder edge. Results showed that the SSP measured using a large test object is dependent on the orbital phase of the helical scan. This obstacle can be mitigated by use of phase-controlled multiple scans. The repeatability of the table position is better than the specifications, enabling the use of ensemble-averaged images for the SSP measurement under extremely low-CNR conditions. By using ensemble-averaged images together with the above method, accurate SSP measurement can be performed even when the test object is visually indistinct against a noisy background. This measurement method, when applied to three different IR methods (AIDR-3D, FIRST, and ASiR-V), successfully revealed the detail of their notable thickening of low-CNR SSP. Their dependences on noise and contrast highly varied between reconstruction algorithms.

Acknowledgments

This work was supported by JSPS KAKENHI Grants 24601003 and 15K09883. Parts of this work were presented at the 100th Scientific Assembly of Radiological Society of North America in Chicago (2014) and at the 42nd Autumn Meeting of Japanese Society of Radiological Technology in Sapporo (2014).

Ethical statement

This research was not performed on animal or human samples; therefore, it does not involve animal and human ethical issues and informed consent.

Appendix. : Data processing for obtaining an SSP from disk images

The entire process explained below was executed using Mathematica [35] code written by us.

A.1. Disk position detection and alignment

K slices are selected from regular-pitched axial images so that a disk is located roughly at its center. An ROI of $I \times J$ pixels is set. Typically, the ROI is a square that is inscribed in a disk image with a margin. The ROI images of K slices constitute a set of three-dimensional data $D_0(i, j, k)$. Then, it is modified to $D(i, j, k)$ by subtracting mean value of μ_1 and μ_K which are the average of all pixels of $D(i, j, 1)$ and $D(i, j, K)$ respectively.

$$D(i, j, k) = D_0(i, j, k) - \frac{1}{2}(\mu_1 + \mu_K) \tag{A1}$$

$D(i, j, 1)$ and $D(i, j, K)$ locate at the both end of k, and their values are mostly governed by acrylic resin and noise. Therefore, $D(i, j, k)$ is base-corrected, but only crudely. This is for ease of subsequent processing. More accurate base-level correction is performed at a later stage.

The position and angle of the disk must be detected before the alignment. The disk is obscured because of low CNR. Fitting of $D(i, j, k)$ using a proper model function $g(i, j, k)$ makes the detection possible. The $g(i, j, k)$ is a Gaussian function in the z-direction. Its center position k_C is a parabolic function of i and j.

$$g(i, j, k) = c_0 \cdot \exp\left[\frac{-(k - k_C)^2}{2\sigma^2}\right] + c_1 \tag{A2}$$

$$k_C(i, j) = c_2 i + c_3 i^2 + c_4 j + c_5 j^2 + c_6 \tag{A3}$$

Actually, k_C can be expressed without the square terms because the disk curvature is negligibly small. However, the square terms can indicate the fitting accuracy. If the obtained square terms are not negligibly small, then the detected disk position might be inaccurate. Such circumstances might occur under extremely low-CNR conditions. In such cases, the images of lower noise, such as those of higher tube current, can be used as surrogates for fitting. In this study, we have not used this option for the evaluation of measurement accuracy, for simplicity. However, for the measurement of SSPs of FIRST, we have used FBP images for this fitting. It is because the signal loss by FIRST, depicted in Fig. 14, made the fitting unstable for low-contrast disks.

Using the disk center coordinate $k_C(i, j)$ determined as described above, the following $D'(i, j, k)$ is obtained as the coordinate-shifted version of $D(i, j, k)$. Here, k is not an index any more, but is a real number.

$$D'(i, j, k) = D(i, j, k - k_C(i, j)) \tag{A4}$$

The alignment is now completed because the center of $D'(i, j, k)$ is located exactly at $k = 0$for all i and j. One-dimensional data $D''(k)$ are

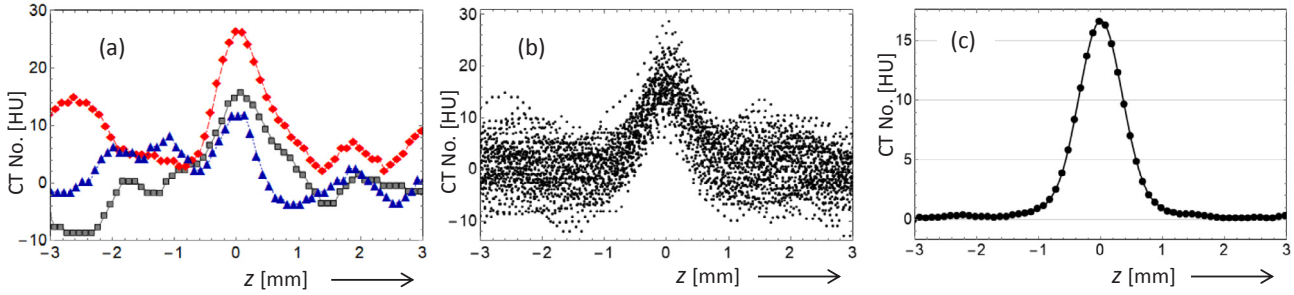

Fig. A1. (a) Individual noisy profiles of three pixels at different positions. (b) Primitive $SSP_0(z)$ consisting of numerous profiles. (c) Binned $SSP_1(z)$ to which base-correction and others are to be applied. These illustrations are a simplification of a real case: $SSP_0(z)$ consists of 16 times more profiles than shown in (b). Data extends far beyond the range shown.

obtained as the union of $D'(i, j, k)$.

$$D''(k) = \bigcup_{i=1}^{I} \bigcup_{j=1}^{J} D'(i, j, k) \tag{A5}$$

Rewriting the coordinate k of $D''(k)$ by $k{\cdot}\Delta z$, where Δz is the pitch of the axial images, we obtain $SSP_0(z)$, a primitive form of SSP. Profiles obtained from single pixels may be extremely noisy (Fig. A1(a)). Collection of all profiles within the ROI is the $SSP_0(z)$ which consists of $I \times J$ profiles (Fig. A1(b)).

$$SSP_0(z) = D''(k{\cdot}\Delta z) \tag{A6}$$

A.2. Binning, base correction, truncation, and width correction

Data that constitute $SSP_0(z)$ are noisy and overly numerous. Regular-pitched and noise-suppressed $SSP_1(z)$ is obtained by binning of $SSP_0(z)$ with bin-size of w (Fig. A1(c)).

Because of shading and other factors, the base level of $SSP_1(z)$ is not zero. Accurate base level correction is extremely important at low-CNR. Regions beyond distance d from the disk center are used for the appraisal of the base level. Regions at both sides are fitted using a linear function. Its subtraction from $SSP_1(z)$ yields the base-corrected $SSP_2(z)$.

$$\mathrm{base}(z) = a + b{\cdot}z \tag{A7}$$

$$SSP_2(z) = SSP_1(z) - \mathrm{base}(z) \tag{A8}$$

The outer regions of $SSP_2(z)$ bear no useful information. $SSP_3(z)$ is obtained by replacing values beyond truncation distance t from the center of $SSP_2(z)$ with zeroes.

Common values are ordinarily used for base-level appraisal distance d and truncation distance t. The value is determined visually as the position at which the foot of $SSP_1(z)$ vanishes sufficiently. However, the observation cannot be accurate at low-CNR. The subtle foot of the SSP should neither be included in the base-level appraisal region nor be truncated. Therefore, we add some margin. For example, a visually sufficient value was 1.5 mm in this study, but we chose 2 mm. An overly large value for d is undesirable because the reduction in the base-level appraisal region results in increased statistical uncertainty of the detected base level at low-CNR.

$SSP_3(z)$ is slightly thicker than true SSP. First, the disk should be infinitely thin, but it has a finite thickness. Second, the binning operation is accompanied by a filtering effect. These effects are corrected for best accuracy. The final SSP is obtained using the correction performed in the Fourier domain as follows.

$$SSP(z) = F^{-1}[C(f_z){\bullet}F[SSP_3(z)]] \tag{A9}$$

$$C(f_z) = \min\left(\frac{1}{S(f_z){\bullet}W(f_z)}, c\right) \tag{A10}$$

$$S(f_z) = \frac{sin(\pi s f_z)}{\pi s f_z} \tag{A11}$$

$$W(f_z) = \frac{sin(\pi w f_z)}{\pi w f_z} \tag{A12}$$

F and F^{-1} denote the Fourier transform and inverse Fourier transform. f_z represents the z-directional spatial frequency. S and W represent the frequency responses of disk thickness s and bin size w respectively. Crepresents the correction function. It is clipped at c to stabilize the correction because the denominator $S(f_z){\bullet}W(f_z)$ approaches zero at high frequency. In this study, c was set as 2.

Appendix A. Supplementary data

Supplementary data to this article can be found online at https://doi.org/10.1016/j.ejmp.2019.03.010.

References

[1] American Association of Physicists in Medicine. Phantoms for Performance Evaluation and Quality Assurance of CT Scanners. AAPM Report No. 1, New York, 1977.

[2] Polacin A, Kalender WA, Brink J, Vannier MA. Measurement of slice sensitivity profiles in spiral CT. Med. Phys. 1994;21:133–40.

[3] Mackie A, Hart GC, Williams-Butt JF. Ramp test objects for slice sensitivity profile measurement in spiral CT. Br. J. Radiol. 1997;70:942–5.

[4] Pahn G, Skornitzke S, Schlemmer H, Kauczor H, Stiller W. Toward standardized quantitative image quality (IQ) assessment in computed tomography (CT): a comprehensive framework for automated and comparative IQ analysis based on ICRU Report 87. Phys. Med. 2016;32:104–15.

[5] Kijewski MF, Judy PF. The noise power spectrum of CT images. Phys. Med. Biol. 1987;32:565–75.

[6] Willemink MJ, Noël PB. The evolution of image reconstruction for CT—from filtered back projection to artificial intelligence. Eur. Radiol. 2018. https://doi.org/10.1007/s00330-018-5810-7 accessed Feb 2019.

[7] Richard S, Husarik DB, Yadava G, Murphy SN, Samei E. Towards task-based assessment of CT performance: system and object MTF across different reconstruction algorithms. Med. Phys. 2012;39:4115–22.

[8] Samei E, Richard S. Assessment of the dose reduction potential of a model-based iterative reconstruction algorithm using a task-based performance metrology. Med. Phys. 2015;42:314–23.

[9] Köhler T, Proksa R. Noise properties of maximum likelihood reconstruction with edge-preserving regularization in transmission tomography. Proc. Fully 2009;3D:263–6.

[10] Mori I. Non-linear Nature of Recent CT Images and Image Quality Evaluation. Bulletin of School of Health Sciences Tohoku University; 2013. p. 7–24. (in Japanese).

[11] Jin H, Kim J. Noise level and contrast dependent behavior of MTF in iterative reconstruction CT imaging. Med. Phys. 2012;39:3636–7.

[12] Yu L, Chen B, Kofler J, Favazza C, Leng S, Kupinski M, et al. Correlation between a 2D channelized Hotelling observer and human observers in a low-contrast detection task with multislice reading in CT. Med Phys. 2017;44:3990–9.

[13] Racine D, Ba A, Ott J, Bochud F, Verdun F. Objective assessment of low contrast detectability in computed tomography with channelized hotelling observer. Phys. Med. 2016;32:76–83.

[14] Joemai RM, Veldkamp WJ, Kroft LJ, Hernandez-Giron I, Geleijns J. Adaptive iterative dose reduction 3D versus filtered back projection in CT: evaluation of image quality. Am. J. Roentgenol. 2013;201(6):1291–7.

[15] Mori I, Machida Y. Deriving the modulation transfer function of CT from extremely noisy edge profiles. Radiol. Phys. Technol. 2009;2:22–32.

[16] Sanders J, Hurwitz L, Samei E. Patient-specific quantification of image quality: an automated method for measuring spatial resolution in clinical CT images. Med. Phys. 2016;43:5330–8.

[17] Takata T, Ichikawa K, Mitsui W, Hayashi H, Minehiro K, Sakuta K, et al. Object shape dependency of in-plane resolution for iterative reconstruction of computed tomography. Phys. Med. 2017;33:146–51.

[18] Tominaga C, Azumi H, Goto M, Taura M, Homma N, Mori I. Tilted-wire method for measuring resolution properties of CT images under extremely low-contrast and high-noise conditions. Radiol. Phys. Technol. 2018;11:125–37.

[19] Urikura A, Ichikawa K, Hara T, Nishimaru E, Nakaya Y. Spatial resolution measurement for iterative reconstruction by use of image-averaging techniques in computed tomography. Radiol. Phys. Technol. 2014;7:358–66.

[20] Yu L, Vrieze TJ, Leng S, Fletcher JG, McCollough CH. Technical Note: Measuring contrast- and noise-dependent spatial resolution of an iterative reconstruction method in CT using ensemble averaging. Med. Phys. 2015;42:2261–7.

[21] Hsieh S, Chesler D, Fleischmann D, Pelc N. A limit on dose reduction possible with CT reconstruction algorithms without prior knowledge of the scan subject. Med. Phys. 2016;43:1361–8.

[22] Chen B, Christianson O, Wilson JM, Samei E. Assessment of volumetric noise and resolution performance for linear and nonlinear CT reconstruction methods. Med. Phys. 2014;41. 071909.

[23] Li K, Garrett J, Ge Y, Chen GH. Statistical model based iterative reconstruction (MBIR) in clinical CT systems. Part II. Experimental assessment of spatial resolution performance. Med. Phys. 2014;41:071911. https://doi.org/10.1118/1.4884038.

[24] Bartolac S, Clackdoyle R, Noo F, Siewerdsen J, Moseley D, Jaffray D. A local shift-variant Fourier model and experimental validation of circular cone–beam computed tomography artifacts. Med. Phys. 2009;36:500–12.

[25] Yamashita M, Yamashita A. A new method for evaluation of slice sensitivity profiles (SSPz) for spatial variation in 64-channel MSCT. Proc. SPIE 2007;6510:65104N.

[26] Hara T, Tsuzaka M, Sakurai N. Measurement of modulation transfer function in Z-axis for multi-slice spiral CT using the micro-disk method: comparison with the bead method and examination of geometric influence. Jpn. J. Radiol. Technol. 2003;59:1391–8. (in Japanese).

[27] Kawata Y, Nakaya Y, Niki N, Ohmatsu H, Eguchi K, Kaneko M, Moriyama N. Measurement of three-dimensional point spread functions in multidetector-row CT. Proc. SPIE 6913, Medical Imaging. Phys. Med. Imag. 2008. https://doi.org/10.1117/12.770861.

[28] Wallihan D, Podberesky D, Sullivan J, Denson A, Zhang B, Salisbury C, et al. Diagnostic performance and dose comparison of filtered back projection and adaptive iterative dose reduction three-dimensional CT enterography in children and young adults. Radiology 2015;276:233–42.

[29] Maeda E, Tomizawa N, Kanno S, Yasaka K, Kubo T, Ino K, et al. The feasibility of Forward-projected model-based Iterative Reconstruction SoluTion (FIRST) for coronary 320-row computed tomography angiography: a pilot study. J. Cardiovasc. Comput. Tomogr. 2017;11:40–5.

[30] Higaki T, Tatsugami F, Fujioka C, Sakane H, Nakamura Y, Baba Y, et al. Visualization of simulated small vessels on computed tomography using a model-based iterative reconstruction technique. Data Brief. 2017;13:437–43.

[31] Hassani C, Ronco A, Prosper A, Dissanayake S, Cen S, Lee C. Forward-projected model-based iterative reconstruction in screening low-dose chest CT: comparison with adaptive iterative dose reduction 3D. Am. J. Roentgenol. 2018;211:548–56.

[32] Kwon H, Cho J, Oh JD, Kim D, Cho J, Kim S, Lee S, Lee J. The adaptive statistical iterative reconstruction-V technique for radiation dose reduction in abdominal CT: comparison with the adaptive statistical iterative reconstruction technique. Br. J. Radiol. 2015;88(1054). 20150463.

[33] Euler A, Solomon J, Marin D, Nelson R, Samei E. A third-generation adaptive statistical iterative reconstruction technique: phantom study of image noise, spatial resolution, lesion detectability, and dose reduction potential. Am. J. Roentgenol. 2018;210:1301–8.

[34] Marco P, Origgi D. New adaptive statistical iterative reconstruction ASiR-V: assessment of noise performance in comparison to ASiR. J. Appl. Clin. Med. Phys. 2018 Mar;19(2):275–86.

[35] Wolfram Research, Inc., Mathematica version 10.3, Wolfram Research, Inc., Champaign, Illinois, 2015.